Energy Storage Materials 25 (2020) 376–381

Contents lists available at ScienceDirect

Energy Storage Materials

journal homepage: www.elsevier.com/locate/ensm

Compact Sn/SnO_2 microspheres with gradient composition for high volumetric lithium storage

Lei Zhang [a,1], Kangning Zhao [a,1], Congli Sun [a,1], Ruohan Yu [a], Zechao Zhuang [a], Jiantao Li [a], Weina Xu [b], Chongmin Wang [c,**], Wangwang Xu [d], Liqiang Mai [a,*]

[a] State Key Laboratory of Advanced Technology for Materials Synthesis and Processing, International School of Materials Science and Engineering, Wuhan University of Technology, Wuhan, 430070, China
[b] Department of Applied Physics, State Key Laboratory of Power Transmission Equipment & System Security and New Technology, Chongqing University, Chongqing, 400044, China
[c] Environmental and Molecular Sciences Laboratory (EMSL), Pacific Northwest National Laboratory, Richland, Washington, 99352, USA
[d] Department of Mechanical and Industrial Engineering, Louisiana State University, Baton Rouge, LA, 70830, USA

ARTICLE INFO

Keywords:
Tin oxide
Volumetric performance
Lithium ion battery
Concentration gradient

ABSTRACT

Volumetric performance of lithium ion batteries becomes increasingly significant in applications of miniaturized consumer electronics, such as cellphones. Herein, we report a successful design of compact Sn/SnO_2 microspheres with a concentration gradient assembled by nanoparticles to realize high volumetric performance. In the structure, the secondary microsphere is able to offer more compact space in realizing higher volumetric capacity. The primary nanoparticles condense together, leading to a dense and porous structure, which can provide more efficient utilization of volume as well as effectively minimize volume variation. Due to the utilization of microstructure as well as the concentration gradient structure, the concentration gradient Sn/SnO_2 microspheres deliver a high volumetric capacity (1593 mAh cm^{-3} at 200 mA g^{-1} after 200 cycles), outstanding rate capability (retaining a capacity of 1230 mAh cm^{-3}), and stable cycling performance (a capacity retention of 97% after 900 cycles at 5 A g^{-1}). This concentration gradient microsphere structure not only provide a high performance conversion-type composite anode, but also a strategy to engineer the energy density of anode materials in compact space towards high energy density.

Concerns over the increasing energy consumption per capita and fast development of new energy intermittent sources, such as solar and wind or even geothermal energy, stimulate the urgent needs for high performance energy storage device [1–7]. Among the current developing and developed energy storage devices, lithium ion batteries have dominated the energy storage device for portable electronics, electric vehicles, aerospace, and so on [8]. However, the development of lithium ion batteries towards higher energy and power densities, falls short from the rapidly developing of high energy consumption areas, such as electric viechle and portable electronics [9–11]. The electrodes are the limiting factors in determining the perfomance of lithium ion batteries. Notably, graphite as commercial anode materials, with low theoretical mass capacity of 372 mAh g^{-1} as well as low volumetric capacity (theoretical 818 mAh cm^{-3}, practical 550 mAh cm^{-3}), lead to a low device energy density (150 Wh kg^{-1}), which does not meet the electric vehicles requirements [12–20]. Thus, it is of great importance to develop new anode materials with high theoretical capacities for the next-generation high energy lithium ion battery [21,22]. Among those, tin oxides have received considerable attentions due to the high energy density and multistep reaction pathway. Typically, tin oxide usually undergoes a conversion reaction ($SnO_2 + 4Li^+ + 4e^- \leftrightarrow Sn + 2Li_2O$) with a potential plateau of ~1.2 V and an alloying reaction ($Sn + xLi^+ + xe^- \leftrightarrow Li_xSn$) at ~ 0.5 V, delivering theriotical capacities of 711 and 783 mAh g^{-1}, respectively. In this way, SnO_2 and Sn are able to deliver theoretical capacities of 1494 and 992 mAh g^{-1}, respectively. However, successfully utilizing the high reversible capacity of SnO_2 is hindered mainly by the disintegration of the electrode structure as well as the poor reversibility of the conversion reaction.

* Corresponding author.
** Corresponding author.
E-mail addresses: Chongmin.Wang@pnnl.gov (C. Wang), mlq518@whut.edu.cn (L. Mai).
[1] These authors contributed equally to this work.

https://doi.org/10.1016/j.ensm.2019.10.003
Received 5 May 2019; Received in revised form 3 October 2019; Accepted 3 October 2019
Available online 7 October 2019

Recently, nanostructured electrodes have been demonstrated a very successful strategy to release the large volume expansion and stablize the electrode/electrolyte interphase of the anode for lithium ion battery. Various nanostructures have been successfully designed and high reversible gravimetric capacities and outstanding cycling stability have been achieved [23–29]. However, when electrode is nanostructured, they often show higher surface area. The nanostructured electrode often shows low tapping density, which leads to low volumetric capacity. Recent progress on tin-based materials, mostly focuses on improvements in the gravimetric capacity and the cycling performance. Moreover, as the volume expansion of tin oxide during the lithiation state is quite high compared with the intercalation electrode, restricting real volumetric performance in application of portable device [30–36]. Another drawback of the nanostructure electrode is that higher surface area would result in more electrolyte decomposition, leading to unsatisfied initial coulombic efficiency. Thus, it is highly desirable to design electrode with combining the advantages of the nanostructured electrode and excellent volumetric performance.

Herein, we report a successful design of compact Sn/SnO_2 microspheres with a concentration gradient (denoted as Sn/SnO_2) assembled by nanoparticles to realize high volumetric performance and high initial coulombic efficiency. In this specially designed structure, Sn is rich inside, contributing to high volumetric capacity while the concentration of SnO_2 is high outside, improving cycling stability. Due to the utilization of microsphere as well as the concentration gradient structure, the Sn/SnO_2 delivers a high initial coulombic efficiency of ~86%, a high volumetric capacity (1593 mAh cm^{-3} at 200 mA g^{-1} after 200 cycles), outstanding rate capability (retaining a capacity of 1230 mAh cm^{-3} at 5 A g^{-1}), stable cycling performance (at 5 A g^{-1}, a capacity retention of 97% is achieved after 900 cycles). Through in-situ and ex-situ characterizations, the secondary microsphere can efficiently make full use of the pore inside and shows much smaller volume expansion compared with the primary aggregates. Additionally, a laddered-type volume expansion is proposed and the strain can be well released along the microsphere, leading to excellent mechanic integrity and cycling stability. It is believed that the advantages above make compact Sn/SnO_2 microspheres a promising alternative for next-generation lithium ion batteries.

1. Discussion

Fig. 1a shows the X-ray diffraction (XRD) pattern of Sn/SnO_2 and two sets of reference patterns, namely, the tetragonal Sn (JCPDS No. 00-004-0673, space group: $I4_1/amd$) and the tetragonal SnO_2 (JCPDS No. 01-077-0447, $P4_2/mnm$), can be well indexed in the pattern. No other peaks are observed, suggesting no other impurities in the composite, except Sn and SnO_2. The crystal structure is investigated through Rietveld refinement implemented by TOPAS 4.2 and the ratio of Sn to SnO_2 is revealed and the weight ratio of Sn is 39.31 wt%. Thus, the molar ratio of $Sn:SnO_2$ is 1:1.2. The morphologies of the samples were then characterized by SEM and TEM. Fig. 1b and c show that the product is composed of uniform microspheres and the size of the sphere is ranging from 0.6 to 2 μm. The microsphere is assembled by nanoparticles aggregations, forming abundant pores. Fig. 1d presents the line profile across a microsphere and the O/Sn ratio gradually increase towards outside, suggesting that metal tin mainly exists inside the microsphere while oxide lies outside the microsphere. Meanwhile, the EDS elemental mapping in Fig. 1d shows that Sn, O, and C were uniformly distributed in the range of the microsphere. The TEM image in Fig. 1e reveals that the microsphere is assembled by nanoparticles. The HRTEM image in Fig. 1f shows the small particle with lattice fringe spacings of 2.78 Å, corresponding to the (101) plane of Sn, and the large particle with the lattice fringe spacings of 2.36 Å, corresponding to the (200) plane of SnO_2, which further confirms that the product is composed of both Sn and SnO_2. The precursor shows a solid microsphere in Figs. S1 and S2, and the pyrolysis of precursor in the air leads to the formation of solid SnO_2 microspheres (denoted as SnO_2) in Figs. S3, S4, and S5. The formation of the Sn/SnO_2 is due to that during the pyrolysis process of Sn/C composite, Sn and carbon would be oxidized simultaneously. However, carbon would be oxidized ahead of the Sn as SnO_2 would also be reduced by carbon. Thus, the Sn/SnO_2 is controlled by the differential oxidation rate of carbon and tin. No carbon is observed in Sn/SnO_2 and SnO_2 microspheres as shown in the Raman spectrum in Fig. S6.

To further identify the chemical state of the Sn/SnO_2, depth profile XPS measurements were carried out and the concentration of Sn and O as well as the Sn/O ratio *vs.* etching time is plotted in Fig. 2a. The oxygen concentration gradually tapers off while the Sn concentration grows higher, further supporting the concentration gradient structure. The Sn/O ratio gradually increases from 0.54 to 6, suggesting that the product is composed of Sn and SnO_2. The Sn 3d XPS spectrum before etching is shown in Fig. 2b. The spectrum indicates the existence of Sn^{4+} (98.6%) as well as a mere part of Sn^0 in the surface of the micrpsphere. However, on the contrast, after 120 min etching, the Sn 3d XPS spectrum shows a vast majority of Sn^0 in the spectrum, suggesting that the inner side of the microsphere is composed of Sn^0. Furthermore, the pore size distribution

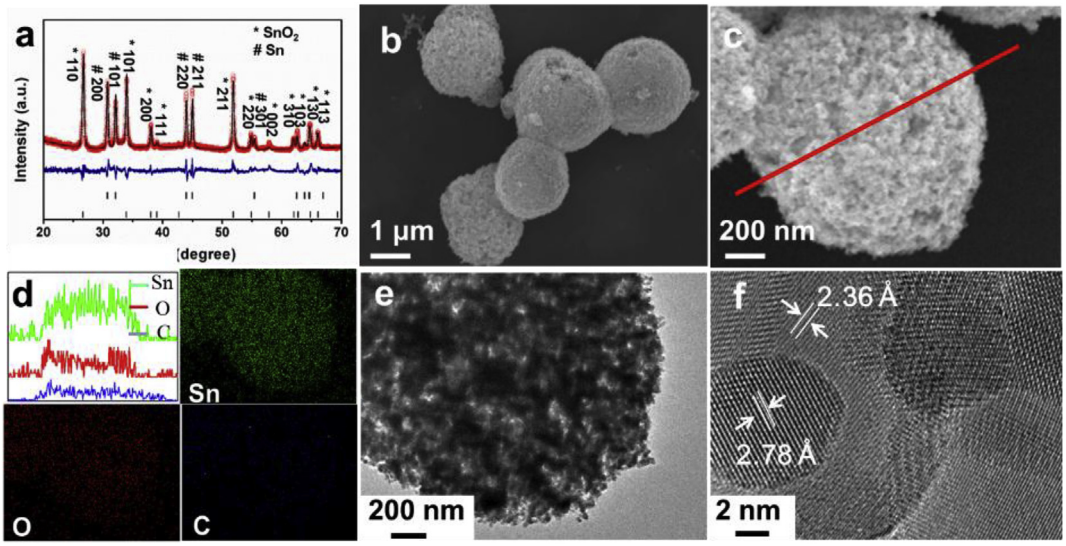

Fig. 1. a) XRD pattern of Sn/SnO_2. b, c) SEM images of Sn/SnO_2 and d) corresponding line scan profile and EDS mapping. e, f) TEM images of Sn/SnO_2.

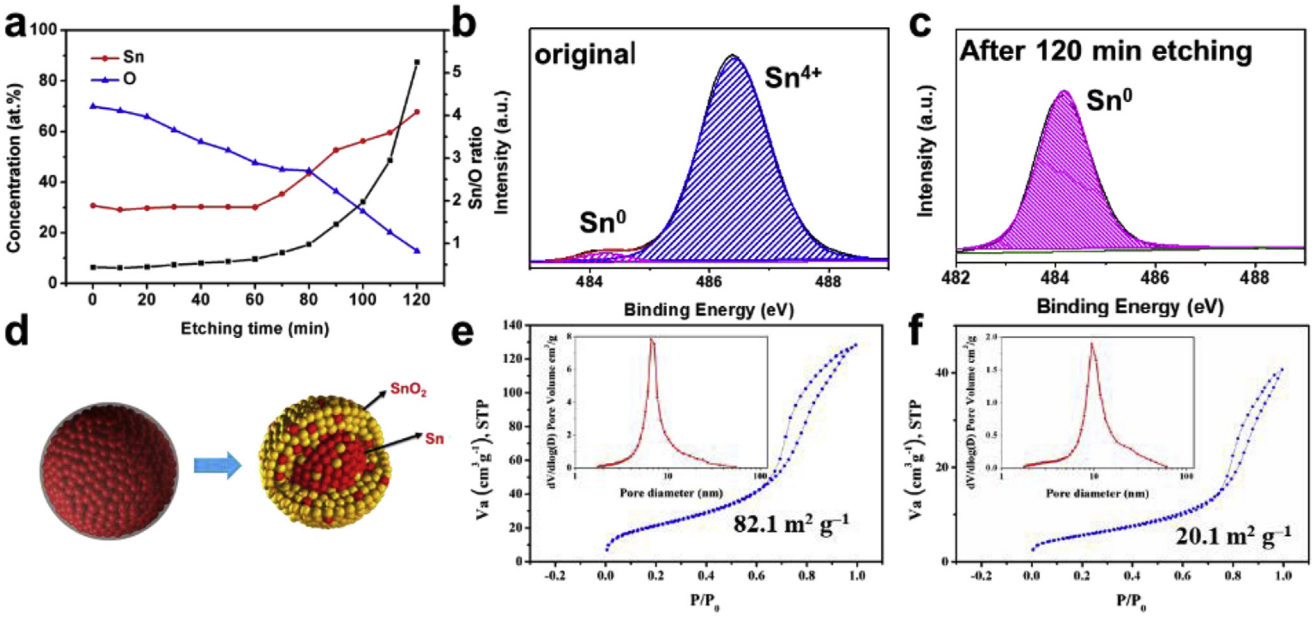

Fig. 2. a) Depth profile of XPS spectra of Sn and O. b, c) Deconvoluted Sn 2p XPS spectra before and after 120-mins etching. d) Schematic illustration of the formation process of Sn/SnO_2. e, f) N_2 adsorption-desorption isotherm curves of Sn/SnO_2 and SnO_2, respectively.

of the Sn/SnO_2 was further investigated (Fig. 2e). The Sn/SnO_2 show specific surface area of 82.1 $m^2 g^{-1}$, the size of the mesopore is ~8 nm. On the contrast, the SnO_2 only show a much lower BET surface area of 20.1 $m^2 g^{-1}$ and the pore size is also larger (~9 nm). The higher surface area is attributed to the reduction process to Sn@C process, leading to more volume in the microsphere.

The electrochemical performance of Sn/SnO_2 is evaluated for lithium storage performance. Fig. S7 shows the cyclic voltammogram (CV) curves of Sn/SnO_2 between 0.01 and 3 V of the initial cycle. During the first cathodic sweep, the peak at 0.76 V is ascribed to conversion reaction of SnO_2 to Li_2O and Sn as well as the formation of SEI [37]. The reduction peak at 0.2 V corresponds to the alloying reaction of Sn with Li to Li_xSn. During the anodic proces, the peaks at range between 0.52-0.67 V and 0.7–0.8 V, which correspond to dealloying process and conversion reaction back to SnO_2, respectively, are separated into two peaks. These two seperated peaks suggest the two different coarsening state of Sn, namely, the Sn derivied from conversion reaction of SnO_2 and the original Sn in the composite [38–40]. The CV curves overlap quite well after 1st cycle, indicating the excellent reversibility of the electrode. To study these non-intercalation electrodes, the electrode thickness is evaluated at different stages including pristine and lithiated state (Fig. S8). The thicknesses of Sn/SnO_2 electrode show much smaller variation (~23%) than that of SnO_2 electrode (~61%). We focus on the volumetric performance of the electrode and the volumetric capacity is shown in the following part. Fig. S9 shows the charging and discharging curves of Sn/SnO_2. The initial capacities of discharge and charge were 2367 and 2047 mAh cm^{-3}, respectively, leading to an initial Coulombic efficiency of 86.5%, which is reproduced as shown in Fig. 3a. The improved Coulombic efficiency is attributed to the increased electrical conductivity and the formation of stable SEI. Fig. 3b shows the cycling performance of Sn/SnO_2 and SnO_2 at 200 mA g^{-1}. It is clearly seen that Sn/SnO_2 exhibits stable cycling performance and retains a reversible capacity of 1593 mAh cm^{-3} after 200 cycles. Meanwhile, coulombic efficiency quickly increases to be above 98% after only 10 cycles. In contrast, the SnO_2 shows high capacity of 1475 mAh cm^{-3} at second cycle, but quickly degrades to below 100 mAh cm^{-3} after only 60 cycles. At 5 A g^{-1}, the coulombic efficiency after 3 cycles quickly increases to above 98%, indicating the stable SEI. Excellent cycling performance is observed and a reversible capacity of 1447 mAh cm^{-3} after 900 cycles is achieved, corresponding to a capacity retention of 97%. The rate capability is further tested at step-increased current densities (Fig. 3d). The Sn/SnO_2 exhibits reversible capacities of 1776, 1663, 1559, 1405, and 1230 mAh cm^{-3} at current densities of 0.2, 0.5, 1.0, 2.0, and 5.0 A g^{-1}, respectively. The capacity retention of 69.2% as the reversible capacities at the currents of 200 mAh g^{-1} relative to 5.0 A g^{-1}. The corresponding gravimetric capacity is shown in Fig. S10. The achieved volumetric and gravimetric capacities outperform those of the current literature reported electrodes [30,41–47] (Fig. S11). The Sn/C shows much lower volumetric and gravimetric capacity due to the high carbon content in Figs. S12 and S13. The EIS of Sn/SnO_2 was carried out to investigate the reaction kinetics (Fig. 3e). According to the fitting results in Table S1, although the R1 value (7.0 Ω) of Sn/SnO_2 is slightly higher than that of SnO_2 (3.9 Ω), the charge transfer resistance value (90.5 Ω) of Sn/SnO_2 is much lower than that of SnO_2 (130.0 Ω). This suggests the enhanced kinetics of Sn/SnO_2.

To further identify the structure integrity, ex-situ SEM and TEM images of the Sn/SnO_2 after 900 cycles are shown in Fig. S14. The SEM image shows that the microsphere is well retained and the corresponding mapping suggest the homogeneous distribution of Sn, O, and C, confirming the excellent structure integrity. Furthermore, we utilized in-situ TEM to analysis the volume expansion during lithiation. Fig. 4a and b show the volume changes of the secondary microsphere and the primary particle in Movie S1 and Movie S2, during lithiation at different reaction time, respectively. The expansion rate is quantified and shown in Fig. 4c. The two microspheres keep stable during the lithiation process and after 268 s, the diameter of the microsphere is increased to its maximum (798 nm), suggesting an expansion rate of 116%. The primary particle in the microsphere is also investigated in Fig. 4b. The primary particle grows from 4.7 to 9.2 nm in 91 s, corresponding to a volume expansion rate of 196%, and keeps stable ever since 91 s. Furthermore, the contact between each primary particle keeps stable and no pulverization or crack is observed in the particles, which suggest the stable microsphere structure. In the structure, the secondary microsphere is able to provide more compact space in realizing higher volumetric capacity. The primary nanoparticles aggregate, leading to a porous structure for sufficient electrolyte contact. First, at initial voltage platform (~0.82 V), the SnO_2 in the Sn/SnO_2 was converted with lithium ions to generate nano Sn(0) and Li_2O as eq (1), while the metallic Sn in the structure remained unreacted:

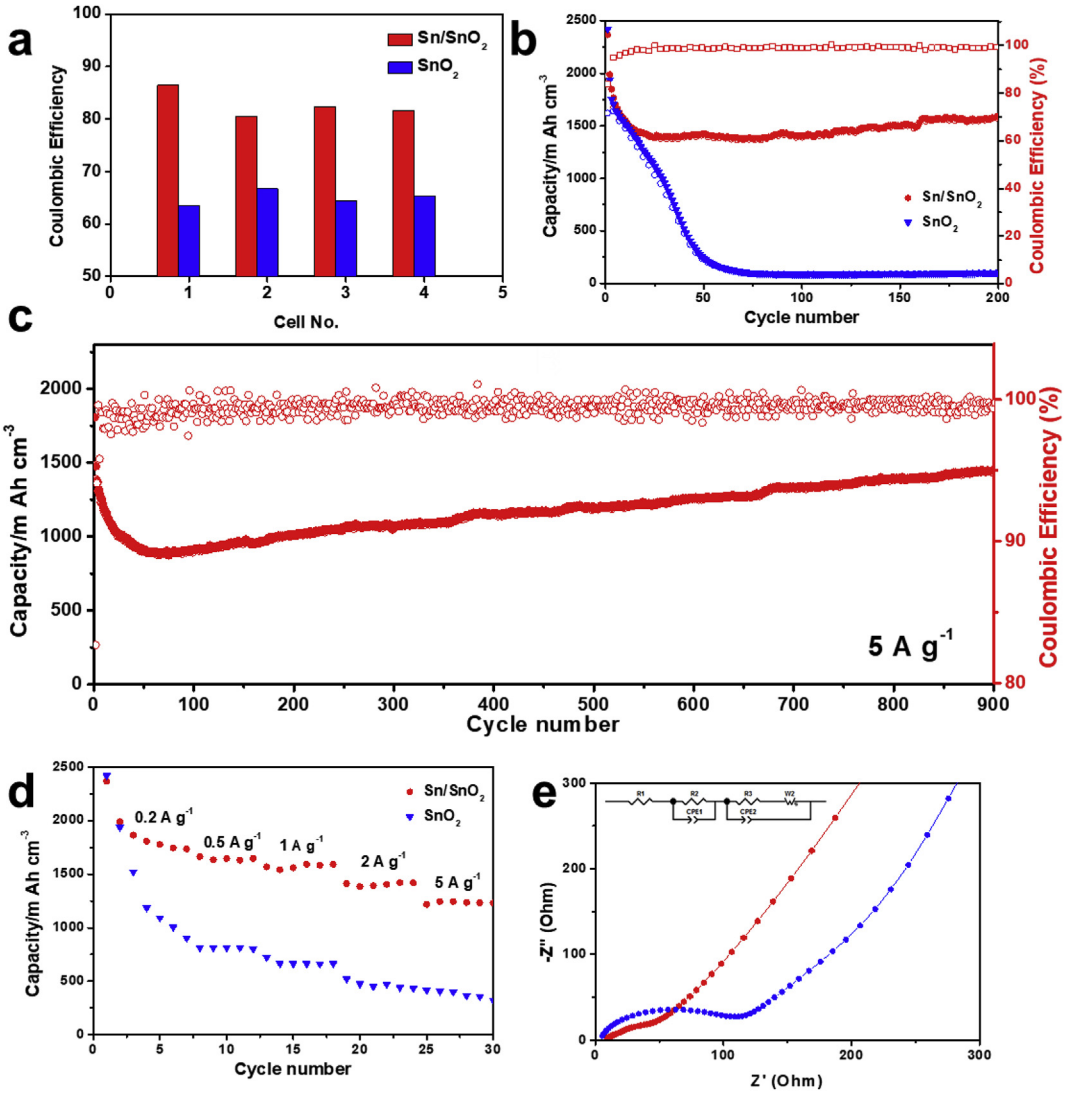

Fig. 3. a) Initial coulombic efficiencies of Sn/SnO_2 and SnO_2. b) The cycling performances of Sn/SnO_2 and SnO_2 at 200 mA g^{-1}. c) Cycling performance of Sn/SnO_2 at 5 A g^{-1}. d) Rate performances of Sn/SnO_2 and SnO_2. e) EIS spectra of Sn/SnO_2 and SnO_2.

$$SnO_2 + 4Li^+ + 4e^- \leftrightarrow Sn + 2Li_2O \quad (1)$$

Supplementary video related to this article can be found at https://doi.org/10.1016/j.ensm.2019.10.003

When the potential dropped to the second voltage platform (~0.45 V), the electrochemically formed nano Sn(0) in Li_2O matrices will undergo the alloying process as eq (2), while other phases including the Li_2O matrices and concomitant Sn phase remain unreacted and act as pillar for better stabilization.

$$Sn + xLi^+ + xe^- \leftrightarrow Li_xSn \quad (2)$$

The concomitant Sn phase undergoes the alloying reaction at 0.35 V. Finally, multiple Li storage mechanisms at the low potential region further lead to the high capacity, including the extra interfacial reaction (surface reaction of LiOH and interfacial lithium and electron storage capacity). It is believed that the inactive components at a certain voltage would act as a buffer zone, to accommodate the volume expansion from the active component upon lithium intercalation. At high voltage where conversion reaction occurs, the inner shell remains inert and act as a buffer zone, to efficiently accomondate the volume expansion of the active outer shell upon lithium intercalation. In this way, the Sn/SnO_2 benefits from the ladder-type buffering effect. Concentration gradient structure is able to offer a ladder-type buffering effect and stablize the structure during discharging when the volume expands [48,49,50].

In conclusion, we have successfully designed and developed a compact concentration gradient Sn/SnO_2 microspheres, which was assembled by nanoparticle aggregates. In the structure, the secondary microsphere is able to provide more compact space in realizing higher volumetric capacity. The primary nanoparticles aggregates, leading to a dense and porous structure, which can provide more efficient utilization of volume and effectively accommodate the volume change, leading to stable lithium storage performance. Due to the utilization of microstructure as well as the concentration gradient structure, the Sn/SnO_2 delivers a high volumetric capacity (1593 mAh cm^{-3} at 200 mA g^{-1} after 200 cycles), outstanding rate capability (retaining a capacity of 1230 mAh cm^{-3} at 5 A g^{-1}), and stable cycling performance (a capacity retention of 97% is achieved even after 900 cycles at 5 A g^{-1}). This concentration gradient microsphere structure not only provides a conversion-type composite anode that allows for excellent electrochemical stability, but also a novel strategy to engineering the packing density for high energy storage capabilities.

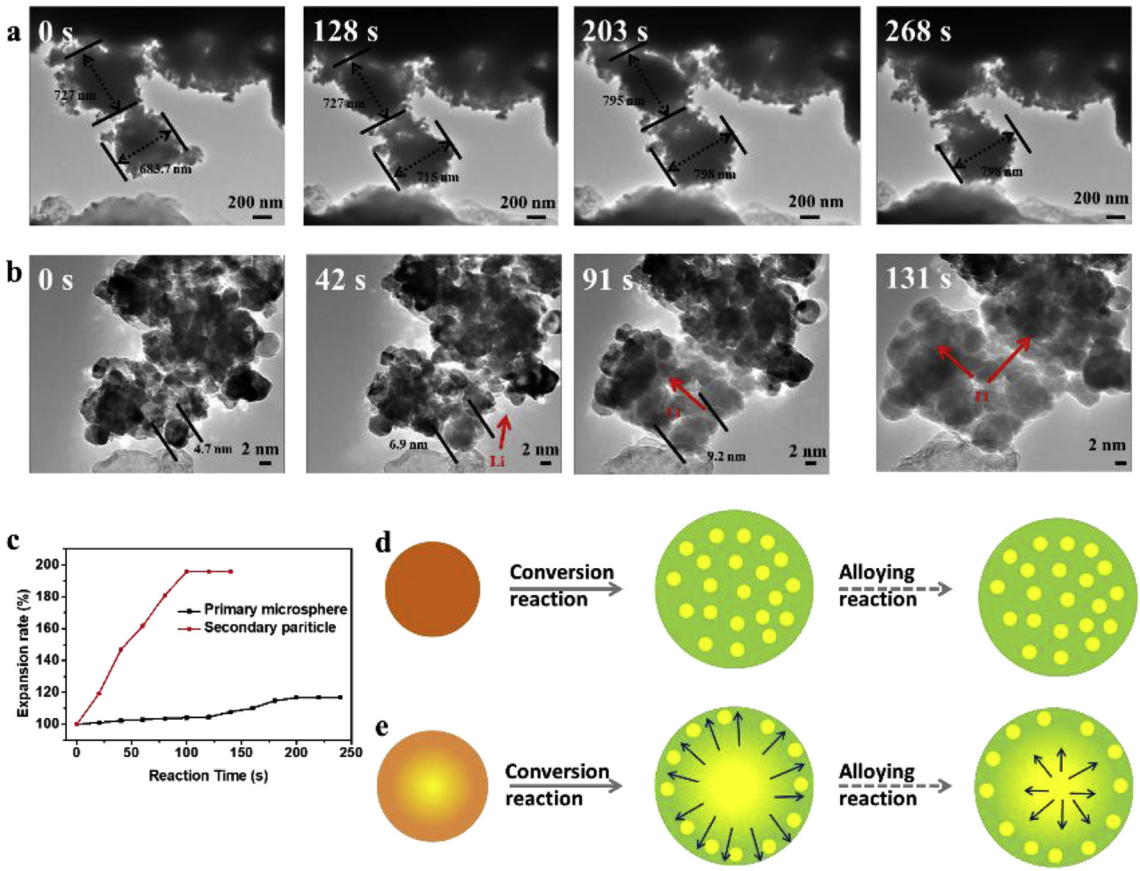

Fig. 4. a, b) In-situ TEM images of secondary microsphere and primary nanoparticles, respectively. c) The volume expansion *vs.* reaction time of secondary microsphere and primary nanoparticles. d, e) Schemetic illustrations of the ladder-type gradient volume expansion process of the Sn/SnO_2.

Acknowledgements

This work was supported by the National Key Research and Development Program of China (2016YFA0202603), the Programme of Introducing Talents of Discipline to Universities (B17034), the National Natural Science Foundation of China (51521001, 21905169, and 51602239), the National Natural Science Fund for Distinguished Young Scholars (51425204), the Yellow Crane Talent (Science & Technology) Program of Wuhan City, and the Hubei Provincial Natural Science Foundation of China (2016CFB267).

Appendix A. Supplementary data

Supplementary data to this article can be found online at https://doi.org/10.1016/j.ensm.2019.10.003.

References

[1] K. Zhao, C. Wang, Y. Yu, M. Yan, Q. Wei, P. He, Y. Dong, Z. Zhang, X. Wang, L. Mai, Adv. Mater. Interf. (2018) 1800848.
[2] L. Pei, Q. Zhao, C. Chen, J. Liang, J. Chen, ChemElectroChem 2 (2015) 1652.
[3] J. Qian, D. Qiao, X. Ai, Y. Cao, H. Yang, Chem. Commun. 48 (2012) 8931.
[4] J. Qian, X. Wu, Y. Cao, X. Ai, H. Yang, Angew. Chem. Int. Ed. 52 (2013) 4633.
[5] L. Wang, X. He, J. Li, W. Sun, J. Gao, J. Guo, C. Jiang, Angew. Chem. Int. Ed. 51 (2012) 9034.
[6] Yujie Zhu, Yang Wen, Xiulin Fan, Tao Gao, Fudong Han, Chao Luo, Sz-Chian Liou, C. Wang, ACS Nano 9 (2015) 3254.
[7] C. Zhang, X. Wang, Q. Liang, X. Liu, Q. Weng, J. Liu, Y. Yang, Z. Dai, K. Ding, Y. Bando, J. Tang, D. Golberg, Nano Lett. 16 (2016) 2054.
[8] J. Newman, C.A. Bonino, J.A. Trainham, Annual Rev. Chem. Biomol. Eng. 9 (2018) 153.
[9] K. Wu, K. Du, G. Hu, J. Mater. Chem. 6 (2018) 1057.
[10] K. Wu, K. Du, G. Hu, J. Mater. Chem. 6 (2018) 3444.
[11] K. Wu, D. Liu, Y. Tang, Electrochim. Acta 263 (2018) 515.
[12] K. Zhao, L. Zhang, R. Xia, Y. Dong, W. Xu, C. Niu, L. He, M. Yan, L. Qu, L. Mai, Small 12 (2016) 588.
[13] S. Chu, A. Majumdar, Nature 488 (2012) 294.
[14] V. Etacheri, G.A. Seisenbaeva, J. Caruthers, G. Daniel, J.-M. Nedelec, V.G. Kessler, V.G. Pol, Adv. Energy Mater. 5 (2015) 1401289.
[15] K.G. Gallagher, S. Goebel, T. Greszler, M. Mathias, W. Oelerich, D. Eroglu, V. Srinivasan, Energy Environ. Sci. 7 (2014) 1555.
[16] J. Liang, X.-Y. Yu, H. Zhou, H.B. Wu, S. Ding, X.W.D. Lou, Angew. Chem. Int. Ed. 53 (2014) 12803.
[17] W. Xu, K. Zhao, C. Niu, L. Zhang, Z. Cai, C. Han, L. He, T. Shen, M. Yan, L. Qu, L. Mai, Nano Energy 8 (2014) 196.
[18] S. Yang, W. Yue, J. Zhu, Y. Ren, X. Yang, Adv. Funct. Mater. 23 (2013) 3570.
[19] X. Zhou, L.-J. Wan, Y.-G. Guo, Adv. Mater. 25 (2013) 2152.
[20] Z. Zhu, S. Wang, J. Du, Q. Jin, T. Zhang, F. Cheng, J. Chen, Nano Lett. 14 (2014) 153.
[21] Q. Xu, J.-K. Sun, Y.-X. Yin, Y.-G. Guo, Adv. Funct. Mater. 28 (2018) 1705235.
[22] Q. Xu, J.-K. Sun, Z.-L. Yu, Y.-X. Yin, S. Xin, S.-H. Yu, Y.-G. Guo, Adv. Mater. 30 (2018) 1707430.
[23] K. Zhao, F. Liu, C. Niu, W. Xu, Y. Dong, L. Zhang, S. Xie, M. Yan, Q. Wei, D. Zhao, L. Mai, Adv. Sci. 2 (2015) 1500154.
[24] K. Zhao, M. Wen, Y. Dong, L. Zhang, M. Yan, W. Xu, C. Niu, L. Zhou, Q. Wei, W. Ren, X. Wang, L. Mai, Adv. Energy Mater. 7 (2017) 1601582.
[25] J. Ryu, T. Chen, T. Bok, G. Song, J. Ma, C. Hwang, L. Luo, H.-K. Song, J. Cho, C. Wang, S. Zhang, S. Park, Nat. Commun. 9 (2018) 2924.
[26] W.J. Chang, S.H. Kim, J. Hwang, J. Chang, D.w. Yang, S.S. Kwon, J.T. Kim, W.W. Lee, J.H. Lee, H. Park, T. Song, I.-H. Lee, D. Whang, W.I. Park, Nat. Commun. 9 (2018) 3461.
[27] L. Fang, Z. Lan, W. Guan, P. Zhou, N. Bahlawane, W. Sun, Y. Lu, C. Liang, M. Yan, Y. Jiang, Energy Storage Mater. 18 (10) (2018) 107–113.
[28] D. Ma, Y. Li, H. Mi, S. Luo, P. Zhang, Z. Lin, J. Li, H. Zhang, Angew. Chem. 57 (2018) 8901.
[29] L. Zhang, K. Zhao, R. Yu, M. Yan, W. Xu, Y. Dong, W. Ren, X. Xu, C. Tang, L. Mai, Small 13 (2017) 1603973.
[30] Y. Dong, B. Wang, K. Zhao, Y. Yu, X. Wang, L. Mai, S. Jin, Nano Lett. (2017), https://doi.org/10.1021/acs.nanolett.7b02698.
[31] J. Han, D. Kong, W. Lv, D.-M. Tang, D. Han, C. Zhang, D. Liu, Z. Xiao, X. Zhang, J. Xiao, X. He, F.-C. Hsia, C. Zhang, Y. Tao, D. Golberg, F. Kang, L. Zhi, Q.-H. Yang, Nat. Commun. 9 (2018) 402.
[32] C. Zhang, W. Lv, Y. Tao, Q.-H. Yang, Energy Environ. Sci. 8 (2015) 1390.

[33] J. Liu, X. Chen, J. Kim, Q. Zheng, H. Ning, P. Sun, X. Huang, J. Liu, J. Niu, P.V. Braun, Nano Lett. 16 (2016) 4501.
[34] T. Ma, X. Yu, H. Li, W. Zhang, X. Cheng, W. Zhu, X. Qiu, Nano Lett. 17 (2017) 3959.
[35] B. Wang, X. Li, T. Qiu, B. Luo, J. Ning, J. Li, X. Zhang, M. Liang, L. Zhi, Nano Lett. 13 (2013) 5578.
[36] N. Liu, Z. Lu, J. Zhao, M.T. McDowell, H.-W. Lee, W. Zhao, Y. Cui, Nat. Nanotechnol. 9 (2014) 187.
[37] Z. Li, J. Ding, D. Mitlin, Acc. Chem. Res. 48 (2015) 1657.
[38] B. Qiu, M. Zhang, L. Wu, J. Wang, Y. Xia, D. Qian, H. Liu, S. Hy, Y. Chen, K. An, Y. Zhu, Z. Liu, Y.S. Meng, Nat. Commun. 7 (2016) 12108.
[39] R. Hu, D. Chen, G. Waller, Y. Ouyang, Y. Chen, B. Zhao, B. Rainwater, C. Yang, M. Zhu, M. Liu, Energy Environ. Sci. 595 (2016).
[40] R. Hu, Y. Ouyang, T. Liang, H. Wang, J. Liu, J. Chen, C. Yang, L. Yang, M. Zhu, Adv. Mater. 29 (2017) 1605006.
[41] J. Luo, X. Tao, J. Zhang, Y. Xia, H. Huang, L. Zhang, Y. Gan, C. Liang, W. Zhang, ACS Nano 10 (2016) 2491.
[42] X. Wang, L. Lv, Z. Cheng, J. Gao, L. Dong, C. Hu, L. Qu, Adv. Energy Mater. 6 (2016) 1502100.
[43] T. Ma, X. Yu, H. Li, W. Zhang, X. Cheng, W. Zhu, X. Qiu, Nano Lett. 17 (2017) 3959.
[44] C. Huang, N.P. Young, J. Zhang, H.J. Snaith, P.S. Granta, Nano Energy 31 (2017) 377.
[45] B.T. Heligman, K.J. Kreder III, A. Manthiram, Joule (2019), https://doi.org/10.1016/j.joule.2019.01.005.
[46] J. Gu, B. Li, Z. Du, C. Zhang, D. Zhang, S. Yang, Adv. Funct. Mater. 27 (2017) 1700840.
[47] L. David, R. Bhandavat, U. Barrera, G. Singh, Nat. Commun. 7 (2016) 10998.
[48] K. Zhao, C. Sun, Y. Yu, Y. Dong, C. Zhang, C. Wang, P.M. Voyles, L. Mai, X. Wang, ACS Appl. Mater. Interfaces 10 (2018) 44376.
[49] J. Yu, Y. Wang, L. Mou, D. Fang, S. Chen, S. Zhang, ACS Nano 12 (2018) 2035.
[50] S. Lian, C. Sun, W. Xu, W. Huo, Y. Luo, K. Zhao, G. Yao, W. Xu, Y. Zhang, Z. Li, K. Yu, H. Zhao, H. Cheng, J. Zhang, L. Mai, Nano Energy 62 (2019) 79–84.